

Femtosecond laser micromachining of fused silica molds

Frédéric Madani-Grasset and Yves Bellouard*

*Mechanical Engineering Department
Eindhoven University of Technology
Eindhoven, The Netherlands
y.bellouard@tue.nl

Abstract The use of low-energy femtosecond laser beam combined with chemical etching has been proven to be an efficient method to fabricate three-dimensional structures in fused silica. For high-volume application, this technology – like other serial processes – suffers from a moderate production rate. Here, we show that femtosecond laser can also be employed to fabricate silica molds and other patterned surfaces, including surfaces with high aspect ratio features (> 10). Through appropriate tailoring of silica's surface property and subsequent creation of, for instance, simple elastomeric molding, new opportunities for the indirect 3D, multi-scale spatial characterization of deep laser-fabricated microstructures come along. We demonstrate that those moldings are characterized by a high fidelity (down to the nanometer scale) to the silica mold. These results further advance the applicability of femtosecond laser processing to glass.

©2010 Optical Society of America

OCIS codes: (320.7130) Ultrafast processes in condensed matter, including semiconductors; (230.4000) Microstructure fabrication; (160.2750) Glass and other amorphous materials; (160.5470) Polymers

References and Links

1. K. M. Davis, K. Miura, N. Sugimoto, and K. Hirao, "Writing waveguides in glass with a femtosecond laser," *Opt. Lett.* **21**(21), 1729–1731 (1996).
2. A. Marcinkevičius, S. Juodkazišius, M. Watanabe, M. Miwa, S. Matsuo, H. Misawa, and J. Nishii, "Femtosecond laser-assisted three-dimensional microfabrication in silica," *Opt. Lett.* **26**(5), 277–279 (2001).
3. S. Nolte, M. Will, J. Burghoff, and A. Tünnemann, "Femtosecond waveguide writing: a new avenue to three-dimensional integrated optics," *Appl. Phys., A Mater. Sci. Process.* **77**(1), 109–111 (2003).
4. A. Szameit, D. Blömer, J. Burghoff, T. Schreiber, T. Pertsch, S. Nolte, A. Tünnemann, and F. Lederer, "Discrete nonlinear localization in femtosecond laser written waveguides in fused silica," *Opt. Express* **13**(26), 10552–10557 (2005), <http://www.opticsinfobase.org/abstract.cfm?URI=oe-13-26-10552>.
5. C. Mauchlaier, G. Cheng, N. Huot, E. Audouard, A. Rosenfeld, I. V. Hertel, and R. Stoian, "Dynamic ultrafast laser spatial tailoring for parallel micromachining of photonic devices in transparent materials," *Opt. Express* **17**(5), 3531–3542 (2009), <http://www.opticsinfobase.org/abstract.cfm?URI=oe-17-5-3531>.
6. Y. Shimotsuma, P. G. Kazansky, J. Qiu, and K. Hirao, "Self-organized nanogratings in glass irradiated by ultrashort light pulses," *Phys. Rev. Lett.* **91**(24), 247405 (2003).
7. E. Bricchi, J. D. Mills, P. G. Kazansky, B. G. Klappauf, and J. J. Baumberg, "Birefringent Fresnel zone plates in silica fabricated by femtosecond laser machining," *Opt. Lett.* **27**(24), 2200–2202 (2002), <http://www.opticsinfobase.org/ol/abstract.cfm?URI=ol-27-24-2200>.
8. M. Beresna, and P. G. Kazansky, "Polarization diffraction grating produced by femtosecond laser nanostructuring in glass," *Opt. Lett.* **35**(10), 1662–1664 (2010), <http://www.opticsinfobase.org/ol/abstract.cfm?URI=ol-35-10-1662>.
9. Y. Bellouard, A. Said, M. Dugan, and P. Bado, "Fabrication of high-aspect ratio, micro-fluidic channels and tunnels using femtosecond laser pulses and chemical etching," *Opt. Express* **12**(10), 2120–2129 (2004), <http://www.opticsinfobase.org/oe/abstract.cfm?URI=oe-12-10-2120>.
10. Y. Bellouard, A. Said, M. Dugan, and P. Bado, "Monolithic three-dimensional integration of micro-fluidic channels and optical waveguides in fused silica," *Materials Research Society Symposium - Proceedings* **782**, 63–68 (2003).
11. Y. Bellouard, A. Said, and P. Bado, "Integrating optics and micro-mechanics in a single substrate: a step toward monolithic integration in fused silica," *Opt. Express* **13**(17), 6635–6644 (2005), <http://www.opticsinfobase.org/abstract.cfm?URI=oe-13-17-6635>.
12. G. Kamlage, T. Bauer, A. Ostendorf, and B. N. Chichkov, "Deep drilling of metals by femtosecond laser pulses," *Appl. Phys., A Mater. Sci. Process.* **77**, 307–310 (2003).

13. Y. V. White, X. Li, Z. Sikorski, L. M. Davis, and W. Hofmeister, "Single-pulse ultrafast-laser machining of high aspect nano-holes at the surface of SiO₂," *Opt. Express* **16**(19), 14411–14420 (2008), <http://www.opticsinfobase.org/oe/abstract.cfm?URI=oe-16-19-14411>.
14. Z. Wang, K. Sugioka, Y. Hanada, and K. Midorikawa, "Optical waveguide fabrication and integration with a micro-mirror inside photosensitive glass by femtosecond laser direct writing," *Appl. Phys., A Mater. Sci. Process.* **88**(4), 699–704 (2007).
15. R. M. Vazquez, R. Osellame, D. Nolli, C. Dongre, H. van den Vlekkert, R. Ramponi, M. Pollnau, and G. Cerullo, "Integration of femtosecond laser written optical waveguides in a lab-on-chip," *Lab Chip* **9**(1), 91–96 (2009).
16. Y. Bellouard, E. Barthel, A. A. Said, M. Dugan, and P. Bado, "Scanning thermal microscopy and Raman analysis of bulk fused silica exposed to low-energy femtosecond laser pulses," *Opt. Express* **16**(24), 19520–19534 (2008), <http://www.opticsinfobase.org/oe/abstract.cfm?URI=oe-16-24-19520>.
17. S. Kiyama, S. Matsuo, S. Hashimoto, and Y. Morihira, "Examination of Etching Agent and Etching Mechanism on Femtosecond Laser Microfabrication of Channels Inside Vitreous Silica Substrates," *J. Phys. Chem. C* **113**(27), 11560–11566 (2009).
18. M. Déruelle, M. Tirrell, Y. Marciano, H. Hervet, and L. Léger, "Adhesion energy between polymer networks and solid surfaces modified by polymer attachment," *Faraday Discuss.* **98**, 55–66 (1994).
19. O. Guiselin, "Irreversible adsorption of a concentrated polymer solution," *Europhys. Lett.* **17**(3), 225–230 (1992).
20. A. Mata, A. J. Fleischman, and S. Roy, "Characterization of polydimethylsiloxane (PDMS) properties for biomedical micro/nanosystems," *Biomed. Microdevices* **7**(4), 281–293 (2005).
21. L. Léger, H. Raphaël, and H. Hervet, "Surface-anchored polymer chains: their role in adhesion and friction," *Adv. Polym. Sci.* **138**, 185–225 (1999).
22. F. Madani-Grasset, N. T. Pham, E. Glynos, and V. Koutsos, "Imaging thin and ultrathin organic films by scanning white light interferometry," *Mater. Sci. Eng. B* **152**(1-3), 125–131 (2008).
23. T. McWaid, T. Vorburger, J. F. Song, and D. Chandler-Horowitz, "The effects of thin films on interferometric step height measurements," in: K. Creath, J.E. Grevenkamp (Eds), *Interferometry: Surface Characterization and Testing (SPIE)*, 1776, 2–13 (1992).
24. Y. Xia, and G. M. Whitesides, "Extending microcontact printing as a microlithographic technique," *Langmuir* **13**(7), 2059–2067 (1997).
25. D. Y. Lee, D. H. Lee, H. S. Lim, J. T. Han, and K. Cho, "Chemical and geometrical criteria for the release of elastomeric 1D nanoarrays from porous nanotemplates," *Langmuir* **26**(5), 3252–3256 (2010).
26. E. D. Palick, "Handbook of optical constant of solids," Academic Press Inc, (1985).
27. F. Madani-Grasset, "Polydimethylsiloxane (PDMS) monolayers: morphology, nanostructure, adhesive and frictional properties," PhD thesis, the University of Edinburgh, 161–166 (2005).
28. M. J. Owen, "The surface activity of silicones: a short review," *Ind. Eng. Chem. Prod. Res. Dev.* **19**(1), 97–103 (1980).
29. A. E. Ismail, G. S. Grest, D. R. Heine, M. J. Stevens, and M. Tsige, "Interfacial structure and dynamics of siloxane systems: PDMS-vapor and PDMS-water," *Macromolecules* **42**(8), 3186–3194 (2009).
30. A. Falsafi, S. Mangipudi, and M. J. Owen, "Surface and interfacial properties," in J.E. Mark (Ed), *Physical properties of polymers handbook 2nd ed*, Springer, New-York, USA, 1012–1018 (2007).
31. E. Barthel, "Adhesive elastic contacts: JKR and more," *J. Phys. D Appl. Phys.* **41**(16), 163001 (2008).
32. Y. Bellouard, T. Colomb, C. Depeursinge, M. Dugan, A. A. Said, and P. Bado, "Nanoindentation and birefringence measurements on fused silica specimen exposed to low-energy femtosecond pulses," *Opt. Express* **14**(18), 8360–8366 (2006).
33. Y. Bellouard, V. K. Pahlwani, T. Rohrlack, A. Said, M. Dugan, and P. Bado, Towards a femtosecond laser micromachined opto-fluidic device for detection algae species, in *Commercial and Biomedical Applications of Ultrafast Lasers IX*, Proceedings of SPIE Vol. 7203 (SPIE, Bellingham, WA 2009); Editors: edited by Joseph Neev, Stefan Nolte, Alexander Heisterkamp, Rick P. Trebino, San Jose, United States, 720312, (2009)
34. F. L. Galeener, "Planar rings in glasses," *Solid State Commun.* **44**(7), 1037–1040 (1982).
35. M. Tomozawa, Y. Lee, and Y. Peng, "Effect of uniaxial stresses on silica glass structure investigated by IR spectroscopy," *J. Non-Cryst. Solids* **242**(2-3), 104–109 (1998).
36. A. Agarwal, and M. Tomozawa, "Correlation of silica glass properties with the infrared spectra," *J. Non-Cryst. Solids* **209**(1-2), 166–174 (1997).
37. K. Awazu, and H. Kawazoe, "Strained Si–O–Si bonds in amorphous SiO₂ materials: A family member of active centers in radio, photo, and chemical responses," *J. Appl. Phys.* **94**(10), 6243–6262 (2003).
38. J. W. Chan, T. Huser, S. Risbud, and D. M. Krol, "Structural changes in fused silica after exposure to focused femtosecond laser pulses," *Opt. Lett.* **26**(21), 1726–1728 (2001).
39. D. Krol, "Femtosecond laser modification of glass," *J. Non-Cryst. Solids* **354**(2-9), 416–424 (2008).
40. D. Rayner, A. Naumov, and P. Corkum, "Ultrashort pulse non-linear optical absorption in transparent media," *Opt. Express* **13**(9), 3208–3217 (2005), <http://www.opticsinfobase.org/oe/abstract.cfm?URI=oe-13-9-3208>.

1. Introduction

The machining of glass using non-linear absorption processes associated with femtosecond laser exposure has recently gained considerable interest due to the versatility and three-dimensional nature of the process. Applied to fused silica, femtosecond laser machining can be used to generate a variety of structures such as waveguides [1–5], nanogratings [6], diffractive elements [7, 8], fluidic channels [9] as well as mechanical components such as flexures [11]. Combining exposure to low-energy pulses and a chemical etching step, ‘solid’ structures such as waveguides can be added to other elements, for instance flexures or channels in a single process as was demonstrated in [10, 11]. This opens up new opportunities for the fabrication of integrated micro-systems where optical, mechanical and fluidic functions are embedded in a single substrate (as illustrated for instance in [11, 14, 15, 33]).

Although monolithic integration reduces considerably the number of processing steps and, as a consequence, the production cost, femtosecond laser machining of glass remains serial in nature and, as such, has limited applicability for large to very large scale productions. Furthermore, fused silica is a material that is too expensive for many applications.

To produce large numbers of low-cost micro-parts, plastic molding (or plastic injection) is often a preferred micro-fabrication technique. Moldings of femtosecond laser structures have been reported recently [12, 13]. Although simple in principle, numerous challenges are associated with this production method including de-molding, limited reproducibility, low aspect ratio and poor mold-resolution (i.e. limitations associated with the smallest features that can be transferred through molding).

In this paper, we explore the use of femtosecond laser as a fabrication means for shallow patterned surfaces as well as high-aspect ratio micro-molds with nanoscale resolution. We demonstrate that femtosecond laser processing of fused silica provides high-resolution, high-aspect ratio silica molds of particular interest for microsystems. Notably, we implement a conformal and tailored nanometer-thick release coating of appropriate adhesive and frictional properties.

2. Femtosecond laser micromachined-glass molds: working principle

The process to machine glass molds is outlined in Fig. 1. The two first steps are similar to the one already described in [9] to machine femtosecond laser features in fused silica. Here, we briefly summarize its main features. Technical details related to each of the steps are provided in the subsequent section of this paper.

1/ **Laser exposure:** the substrate is exposed to low energy pulses (typically 150 to 220nJ with a focusing objective of NA equal to 0.45). At these energy levels, no ablation occurs, instead rather internal modifications of the silica structure take place [16, 17, 32], which eventually leads to localized enhanced susceptibility to wet chemical etching. To form a three-dimensional pattern of modified material structure, the substrate is translated in the three-dimensions under the laser-beam. Patterns are created by stitching laser affected-regions together so that a continuous area of upset material structure is being generated [9].

2/ **Mold chemical etching:** the substrate is etched in an aqueous solution of hydrofluoric acid (2.5% to 5%). Those regions that have been exposed to the laser beam are etched faster than the unexposed regions with a typical etching rate ratio of 60 to 1 (i.e. 1 μ m/min for exposed regions versus 1 μ m/hour for unexposed ones). Note that it was recently shown by S. Kiyama *et al.* [17] that hot KOH offers an interesting alternative to HF for this step as it may yield an even higher etching rate ratio (1:200) under certain conditions.

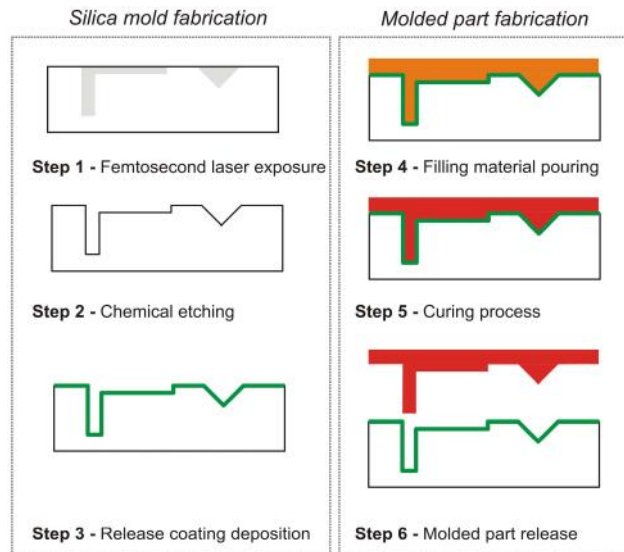


Fig. 1. Overview of the femtosecond mold fabrication process and the fabrication of molded parts.

3/ **Making of the release coating:** nanometer-thick irreversibly adsorbed PDMS monolayers are formed on silica substrates through a physisorption mechanism [18, 19]. The purpose of this layer is to reduce both the adhesion of the molding material with the mold and perhaps more importantly yet their friction upon molding removal, be it manually or in an automated fashion. This step is necessary to ensure successful de-molding, in particular for high-aspect ratio structures and repeated moldings.

4/ **Mold filling:** the material to be molded is being poured (or spin-coated) in its liquid state into the mold. In the present paper, we report on molded elastomeric PDMS structures for demonstration purposes. Stiffer materials such as many thermoplastics, certain thermosets and, obviously, other elastomers could also be considered. In spite of their high compliance ($E_{\text{PDMS}} \approx 1\text{MPa}$ [20]), which can be seen as a major advantage in terms of release, PDMS elastomers are loose networks. Release coating polymeric chains can penetrate the PDMS network creating chain entanglements, which can increase by up to an order of magnitude or more the adherence and friction between the mold and the molding [21]. All things considered, PDMS is a rather challenging molding material. Most thermoplastics and thermosets are not expected to pose such an issue and successful attempts made with PDMS elastomers could be regarded as a solid proof of concept. PDMS chains do degrade irreversibly at temperatures around 200°C , which can be problematic when working with some thermosets. Other release coatings would then have to be used. However, this operating temperature limit is sufficiently high for a great many molding materials.

5/ **Curing and release of the molding:** the mold and its filling are placed in an oven for curing (crosslinking in this case) and subsequent release.

Steps 4 and 5 are repeated for each molded part.

3. Methods

3.1 Laser micromachining and etching: mold fabrication

For these experiments, we use two different laser systems.

A first series of specimens consisting of holes were produced with an oscillator (t-Pulse 500, Amplitude Systèmes based Yb-KGW crystals). It emits 550-fs pulses at 9.4 MHz and at 1030nm. We use an AOM to reduce the repetition rate to sub-MHz values. For these experiments, we worked at 860 kHz which does not produce visible heat-accumulation effects. The specimen is mounted on Physik-Instrument stages and moved under the laser

focal point at a speed of 1mm/s. To focus the beam, we use an objective with a numerical aperture of 0.40. The pulse energy and laser repetition rate was set respectively to 160 nJ and 860 kHz.

A second set of specimens consisting of more complex structures (micro-channels carved out from the glass surface and trenches) were produced with a Ti:Sapphire emitting 100-fs pulses at 250 kHz. There, the writing speed was 2 mm/s and the energy of 200 nJ per pulse. The NA of the focusing objective was 0.45. The specimens were mounted on a translation stages and moved under the microscope objective.

3.2 Release coating: fabrication steps and structure

Nanometer-thick, irreversibly physisorbed polydimethylsiloxane (PDMS) monolayers made up of (α, ω) silanol-terminated macromolecules: $(\text{HO})-(\text{CH}_3)_2\text{-SiO}-(\text{Si}(\text{CH}_3)_2\text{O})_n\text{-Si}(\text{CH}_3)_2\text{-}(\text{OH})$, also known as pseudo-brushes, were grown on silica substrates from commercially available polydisperse PDMS melts (Gelest, Inc). Polydispersity in polymers designates a wide distribution of its chain length or molecular weight about a central value. We selected a compound whose average molecular weight, M_w , was equal to 139 kg mol⁻¹. The growth mechanism can be broken down into several steps:

1/ Deposition step: droplets of highly concentrated PDMS solution in octane solvent (VWR, 99 + %) with a volume fraction close to 50% were quickly and homogeneously deposited onto freshly piranha-cleaned [18, 22] and N₂-dried fused silica substrates of various thicknesses (from 0.5 to 1 mm) in which the femtosecond laser-written patterns were printed.

2/ Solvent evaporation: the samples were left in ambient conditions ($T \approx 20^\circ\text{C}$ and $P \approx 1$ bar) for 12h (covered but not sealed by a clean glass dish) in order for the octane to slowly evaporate without disturbing the polymer chain distribution at the silica surface. At this early stage, the substrates were covered in a 'thick' (\approx a few hundreds of μm) and essentially pure, i.e. solvent-free, PDMS film.

3/ Incubation: the samples were incubated in an oven at 110°C for 24h so as to complete the adsorption process and to get a saturation of the available adsorption sites by polymeric chains in accordance with a protocol set up elsewhere [18].

4/ Rinsing: the macroscopic PDMS excess was rinsed off in toluene using a dedicated wash bottle. Finally, the more subtle removal of the unadsorbed PDMS chains was accomplished by putting the samples in a toluene bath for a minimum of 2h, which left a nanometer-thick PDMS monolayer on the substrate.

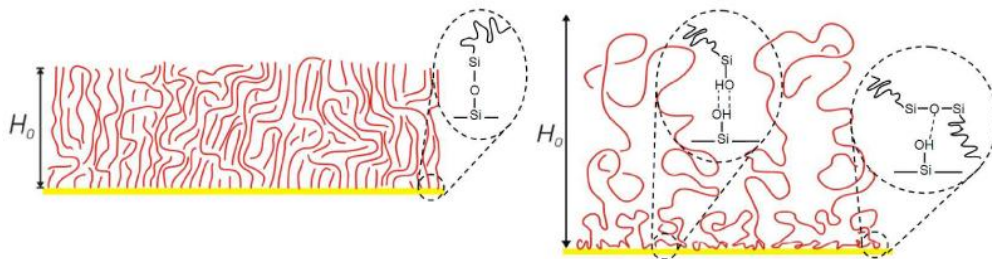


Fig. 2. Schematic of the molecular structure of a polymer brush (left) and a pseudo-brush (right) in good-solvent conditions. H_0 is the brush thickness. A pseudo-brush is made up of loops, tails and trains. Those are closest to the substrate (yellow rectangle). In bad-solvent conditions (such as in air), chains collapse onto the substrate. The fine structure can then be assumed to be dominated by trains with only some shorter loops. We represent the types of attachment at the atomic level, in both the chemisorption (left) and physisorption (right) cases for PDMS on silica. The latter case is less well understood. Although H-bonds are thought to be dominant, simple van der Waals (vdW) forces may play an important role too. Some limited chemisorption through condensation reactions cannot be ruled out either [18, 21].

Schematically, the monolayer looks like a thin and intricate maze of filaments as sketched in Fig. 2. Note that the pseudo-brush structure differs obviously from that of a true, chemisorbed (i.e. end-tethering through covalent bonds) brush in good-solvent conditions as

was predicted theoretically by Guiselin [19]. In bad-solvent conditions, for instance in air (our operating situation), polymer chains collapse onto the substrate surface [18, 21] and the difference in fine structure must then be a lot less ‘clear-cut’. It is important to stress that adherence between a PDMS network (elastomer) and a PDMS brush or pseudo-brush of a particular average chain length depends upon the brush grafting density, i.e. the number of anchored chains per unit area, according to a distorted bell curve [21]. For ‘very high’ grafting densities, chain interdigitation is made more difficult, hence adherence decreases.

3.3 Molding process

PDMS in its elastomeric form (Sylgard 184 silicone from Dow Corning) was utilized as molding material. A pre-polymer consisting of vinyl terminated-PDMS chains was mechanically mixed in ambient conditions with a cross-linking agent (a silane-type molecule) and a catalyst in an inert plastic boat. In order for the mixture to give rise to as stiff and tensile-strong an elastomer as possible, ~15% wt of cross-linker was added to the pre-polymer according to Mata *et al.* [20]. The mixture being full of air, it was degassed in a desiccator for 20 minutes after which it was poured onto the silica samples. The samples were degassed again to get rid of most air bubbles as the mixture was still liquid at this stage and finally cured (here, cross-linked) in an oven at 120°C for 2h.

3.4 Characterization techniques

To measure the PDMS pseudo-brush thickness, which is also a measure of the key parameter that is surface chain density [21], we used an optical profilometer (PL μ 2300, Sensofar) that implements several techniques including phase-shifting interferometry (PSI) in combination with a classical optical microscope. PSI makes use of a monochromatic light beam (in this case, the source emits at $\lambda = 470$ nm) to achieve the best possible lateral resolution in air for a given objective lens. Its resolution in height is lens-independent and of sub-nanometer order [22]. It is known to be extremely roughness-sensitive, particularly on highly flat and smooth surfaces [22, 23]. To compensate for the lack of flatness of the interferometer’s internal mirror at this scale (field of view: 1240 μ m x 930 μ m), a reference, averaged measurement over 9 data collections (improved precision) was made with a certified flatness standard (CVD SiC reference flat, flatness = 0.011 λ , rms roughness = 0.54Å by Rohm & Haas). A layer boundary or edge is necessary for PSI to be effective as a film thickness measuring technique.

The topography of PDMS moldings was measured using confocal scanning microscopy (CSM, also implemented by the above-mentioned instrument PL μ 2300). The technique’s resolution in height – and laterally – is lens-dependent. The former is of the order of 10 nm, like the corresponding accuracy. Very high NA (150x magnification) objectives were used to reach submicron lateral resolution while being able to cope with slopes as high as 70°. Considering first the known ability of PDMS to fill and wet the tiniest cavity or corrugation, a property that has been widely exploited for more than a decade in the field of soft lithography [24, 25], second the PSI measurements revealing the presence of a PDMS monolayer on top of an imperfectly smooth glass surface, third the superb CSM results obtained on high aspect ratio holes chemically etched in fused silica (see the results section for further information), the inverted surface topography of silicone moldings was assumed to be an accurate and dependable enough replica of the original silica surface to justify advanced surface metrology. This way, unreachable inner silica surfaces created through micromachining such as deep holes, were (indirectly) observed and measured. For the first time, we are able to quantitatively assess the surface characteristics as well as other form parameters of deep microstructures. In addition to the above-described micro-/nanotopometry tools, traditional techniques such as scanning electron microscopy (SEM) and classical optical microscopy where used to retrieve further information from the molded structures. For SEM observations, the microstructures were coated with a thin gold-palladium layer.

4. Experimental results

4.1 PDMS monolayer thickness

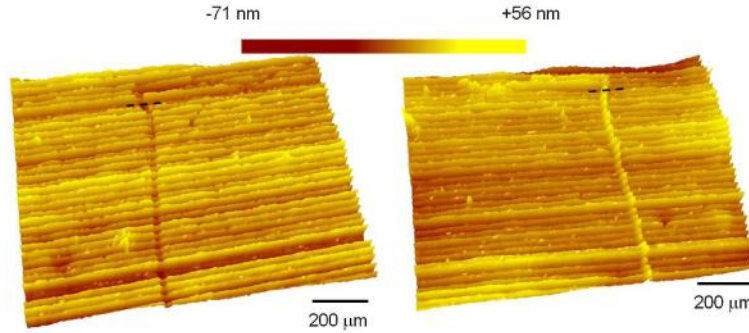


Fig. 3. PSI surface topographic maps of PDMS-coated silica (left) and a PDMS molding of the same sample (right). PDMS being liquid-like and very soft at room temperature, a scratch made with a sharp steel needle (top to bottom orientation) was sufficient to create an edge without affecting in the slightest the topography of the much harder silica substrate (lines oriented lengthwise). The molded scratch appears as a bank (right).

The PSI surface topographic maps presented in Fig. 3 reveal an undulated surface for a particular silica sample. These undulations result from the substrate fabrication process and not the polymeric monolayer growth. Here, they have a periodicity of $\approx 28 \mu\text{m}$, their width ranges from $15 \mu\text{m}$ to $17 \mu\text{m}$ and their height ranges from 15 nm to 30 nm . Though non-ideal, this sample offers a chance to test PSI's surface sensitivity as well as the accuracy (fidelity) of the molding in the nanometer range (height). Some cross-sections were taken on areas about the scratch made through the PDMS overlayer (see Fig. 3) for both mold and molding and height differences between neighboring summits and valleys were measured. We define, Δh , the average error in height difference, as an estimate of the molding's fidelity. We find: $\Delta h = 1.6 \text{ nm}$, a value that is satisfactory although not perfect but multiple reflections-induced artefacts due to the PDMS layer and other sorts of instrumental uncertainties may also have played a part in this. Furthermore, this far from ideal surface roughness does not keep from measuring accurately the PDMS pseudo-brush thickness at all since the step is abrupt enough and PSI extremely surface-sensitive. Step height measurements carried out on the left map show that the polymer monolayer has a thickness of $(10 \pm 0.8) \text{ nm}$, while those made on the right map (molding) reveal a thickness of $(19 \pm 1.5) \text{ nm}$. The discrepancy is related to the fact that PSI being an intensity-sensitive technique, any significant variation in surface refractive index will bring an error into the interferogram conversion process, especially over the film boundary. Such is the case for the 'mold' sample as silica's refractive index is close to 1.45 [26] while that of PDMS in the form of a monolayer was previously measured to be close to 1.55 by ellipsometry [22]. On the other hand, the molding is made of a sole material, providing the desired optical uniformity for accurate thickness measurement. This real thickness value: $(19 \pm 1.5) \text{ nm}$ compares favorably with other experimental data for chains of similar length [18, 21]. Theoretical scaling laws validated by experiments for polymers at surfaces - with PDMS as a model system - give expressions of surface chain densities as well as pseudo-brush thicknesses in bad-solvent conditions [21]:

$$\sigma \cong N^{-\frac{1}{2}} \Phi_0^{\frac{7}{8}} \quad (0.1)$$

where σ is the dimensionless surface chain density, N is the number of monomers per polymeric chain and ϕ_0 is the volume fraction of polymer in the solution (solvent);

$$h_0 \cong aN\sigma \quad (0.2)$$

where h_0 is the thickness of the collapsed or ‘dry’ pseudo-brush (bad-solvent conditions) and a is the monomer size (≈ 0.5 nm for PDMS);

$$h_0 \cong aN^{\frac{1}{2}}\Phi_0^{\frac{2}{3}} \quad (0.3)$$

Although those relationships are scaling laws rather than equations, one can apply scaling law (0.3) to our thickness measurements so as to assess the real average molecular weight of the adsorbed PDMS chains since we started out with a polydisperse sample. We find $M_w^{\text{eff}} \approx 110 \text{ kg mol}^{-1}$ (i.e. ≈ 1486 monomers) as opposed to 139 kg mol^{-1} , which remains close. The surface chain density per unit area, ν ($= \sigma/a^2$), can then easily be estimated from the latter and the thickness using relationship (0.2). We find $\nu \approx 0.104 \text{ chain nm}^{-2}$. Note that expression (0.1) predicts a surface chain density increase with an increase in polymer volume fraction. Results reported in [18, 21] for unit volume fraction samples were actually obtained in two steps: a 10% volume fraction solution was left to evaporate prior to final incubation while we started out with a 50% volume fraction. Our surface chain density might hence be higher than theirs for a given molecular weight. Considering that the measured adherence between a PDMS elastomer and a PDMS pseudo-brush by peel or Johnson-Kendall-Rogers (JKR) tests [31] decreases dramatically with increasing surface chain density [21], this is a benefit. In fact, at high chain density the work of adherence, G , ranges from the mere reversible work of adhesion (here, cohesion) of PDMS, W , which is $(43 \pm 3) \text{ mJ.m}^{-2}$ from careful surface tension component measurements [27–30], to 3.5 times W , depending on the experimental conditions. The upper limit represents at the most a sixth of the adherence measured with less dense, optimized-for-maximum adherence pseudo-brushes. Although less adept at inhibiting adherence than true end-grafted brushes in most situations, high surface chain density pseudo-brushes behave as well as brushes if not better [21], while being much easier to prepare for the non-chemist. All of the above suggests that: we are dealing with a dense, irreversibly adsorbed polymer monolayer in the pseudo-brush form— and not a multilayered structure — whose morphology is bound not to allow interdigitation, making it an adherence or adhesion inhibitor to molding materials including a PDMS elastomer.

4.2 Molded structures of high aspect ratio

To investigate the aspect ratio of our process, holes with various depths from shallow features to troughs about 100 μm -deep were made by translating the substrate along the optical propagation axis. Figure 4 and Fig. 5 show SEM images of an array of holes along with their moldings. Their depth is diverse: some are partially formed, others are ‘incomplete’, the rest run deep down. They are spatially arranged in such a way that the pattern does not have any symmetry. This precaution ensures that there is no ambiguity in matching moldings with molded structures. Both the fused silica mold and its PDMS molding are shown. We note a perfect match between the mold and the molding even for rather deep structures and complex 3D shapes as is illustrated in inset B.

The molding reveals features of aspect ratio (defined here as the pillar length to pillar foot diameter ratio) of up to at least 10 to 1 (inset A in Fig. 4) and possibly higher (inset C in Fig. 4). In addition, a fine undulation, seemingly periodical can also be observed on the PDMS molding only. It is at or below the micron scale laterally. One may ask if this feature is caused by laser to matter interaction, or is it merely a consequence of the Au-Pd film’s intrinsic stress pulling up compliant PDMS. To answer this question, we performed surface roughness (height) calculations in the spatial frequency domain using Fourier Transform procedures to extract the rms roughness, Rq , as well as the periodicity values (distance parameter in the horizontal plane) using flat portions (Fig. 4 white dashed rectangle) or collapsed PDMS pillars (Fig. 5 right: white dashed enclosures).

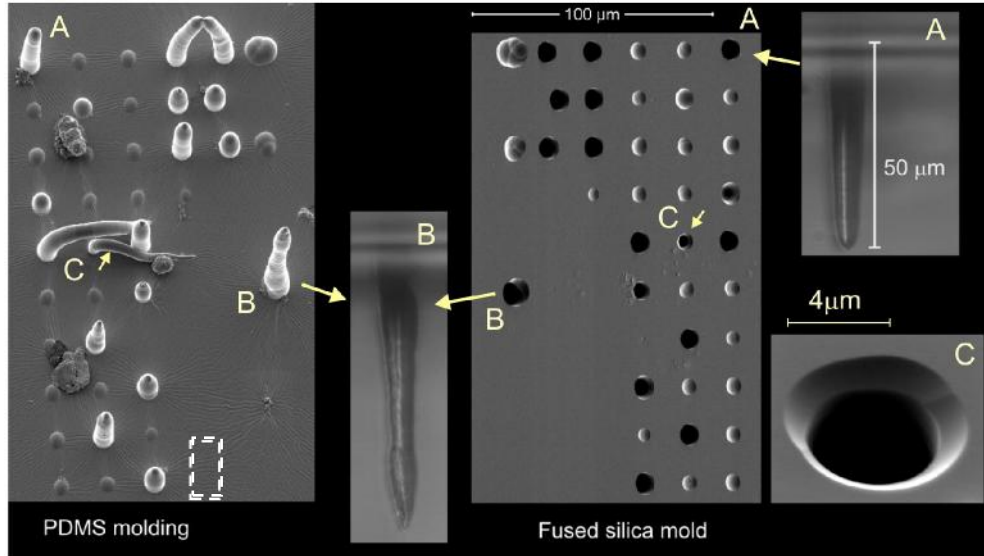


Fig. 4. SEM images of an array of holes of various depths. Insets A and B are optical micrographs taken by looking through the substrate edge. We note a perfect match between the mold and the molding even for rather deep structures and complex shapes as is illustrated in inset B. (dirt is also visible on the PDMS molding, it is due to contamination while handling the specimen and is unrelated to the molding process *per se*.)

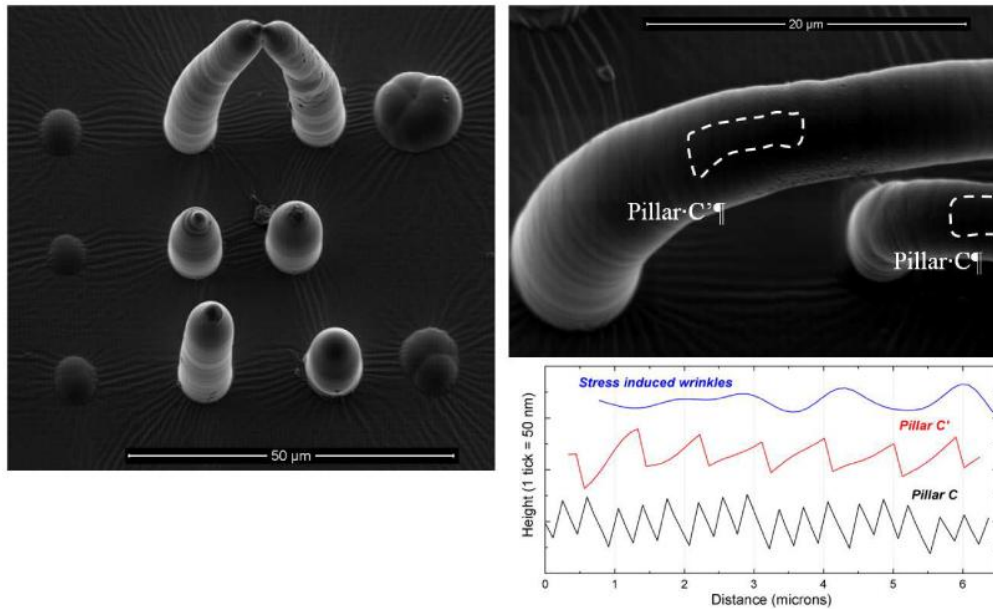


Fig. 5. Moldings of holes of various depth (close-ups of pillars presented in Fig. 4). Two of the longest PDMS pillars collapsed one on another due to their poor mechanical properties and mutually attractive forces. Interesting features resulting from the laser processing are also revealed. We note the presence of oscillations on the pillar radius and oriented along the laser propagation axis. The periodicity is sub-micron for a similar roughness. Wrinkles (or ripples) can be seen on the 'flat' plane. They result from the stress induced by the metal-coating deposited on the PDMS molding for SEM observation (sample preparation artefact).

We found that the intrinsic metal film stress generates an Rq of approximately 17 nm and a periodicity of 1.8 μm . Pillars C and C' show an Rq of 31 nm and 24 nm, respectively, while their periodicity is only 400 nm and 900 nm, respectively. Note that these features seem to be typical of holes (or tunnels) manufactured by femtosecond laser writing followed by wet etching (see [9] where such modulations are also visible). It is unclear though whether this phenomenon originates from the laser writing *per se* - it does seem to be independent of the writing speed - or whether it is a byproduct of the chemical etching. It nevertheless illustrates the nanometer resolution capability of the molding process.

4.3 Thorough quantitative analysis of femtosecond laser micromachined-channel surfaces

As demonstrated in [9], arbitrary patterns can be made by juxtaposing laser-affected zones. The volume to be etched away is scanned with the laser beam so that a pseudo-continuous exposed pattern is formed. For instance, one can carve out a channel structure of arbitrary depth. The ability of making channels with smooth surfaces can be particularly important for certain fluidic and optical applications. Unfortunately, and as a consequence of their high aspect ratio, it is usually not possible to quantitatively assess the floor quality of such deep structures.

To better master the process, it is essential to understand how multiple laser-exposed areas interact with each other so that one can accurately control the final etched profile.

Thanks to their high-fidelity and high resolution (a conservative estimate of a few nanometers as illustrated in Fig. 3 is fair), the use of moldings gives us the opportunity to quantitatively estimate and characterize the surface topology of open fluidic channels be it on the side or bottom wall.

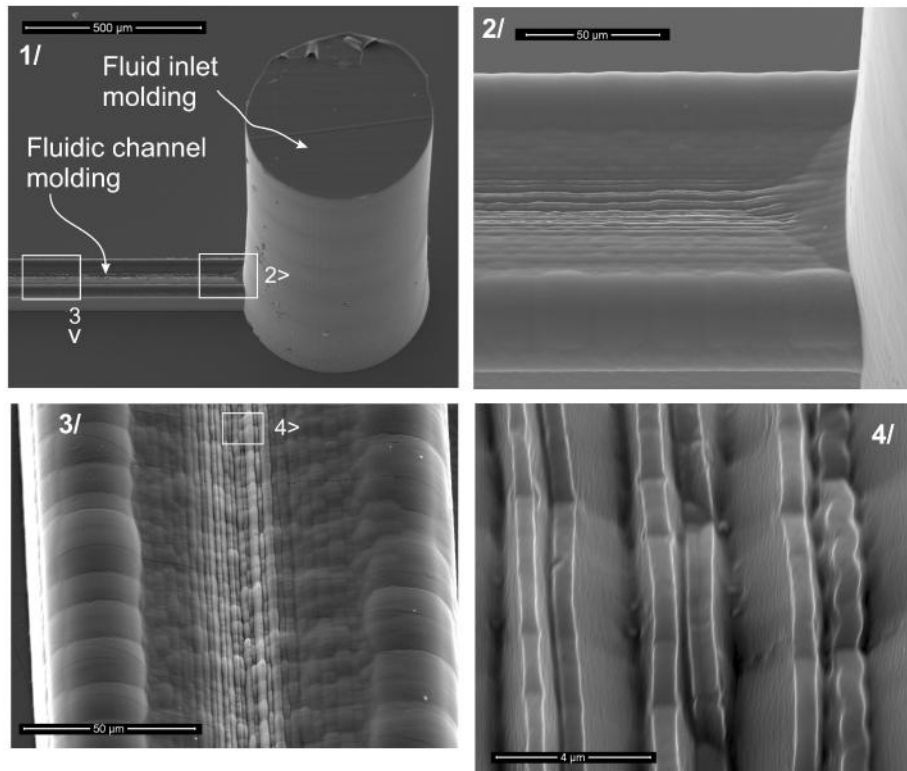


Fig. 6. Molded part consisting of a microchannel and an inlet. Top views: overall snapshot of the structure, bottom views: details of the fluidic channel floor. Fine structure of nanometer size resulting from laser exposure is clearly visible. This example illustrates the use of a molding process to assess the surface quality of a deep structure such as a fluidic channel.

To illustrate this idea, we examine a structure consisting of an elongated fluidic channel (several cm long) connected at both ends to through holes and machined out of a fused silica wafer. The channel has a 100 x 100 micron cross-section and was fabricated with a transverse polarization. This fluidic channel device is described in much detail elsewhere [33]. The channel cross-section was made by juxtaposing laser affected-zones arranged in a U shape, defining the channel contour.

Figure 6 shows the molding of this fluidic device. There, the channel appears as a rectangular wall connected to two 'towers' that are moldings of the inlet and outlet of the fluidic device. A silicon substrate is used as a support for the PDMS molding. Beyond the lack of flatness, the molding reveals roughness consisting of straight lines whose amplitude is in the tens of nanometer scale (see in Fig. 6, insets 3 and 4). This is caused by the laser exposure and the way the sample was moved relative to the beam in accordance with our previous observations [9].

Just like in section 4.2, the channel floor surface topography (corresponding to the top surface of the molded part) as well as the channel side walls topography was carefully processed by Fourier analysis in the spatial frequency domain so as to work out the principal surface texture parameters. From the inverted surface topography maps (to simulate the silica mold surface, shown in Fig. 7), the following quantities were obtained: height parameters, such as the rms roughness, Rq ; a distance parameter in the horizontal plane, namely the feature spacing between mostly troughs or valleys and less often peaks due to the way the surface was processed, i.e. laser exposure and dissolution in HF. Table 1 gathers the most significant data and leaves out figures corresponding to other areas that did not bring in anything new or were polluted by too many cracks in the Au-Pd film.

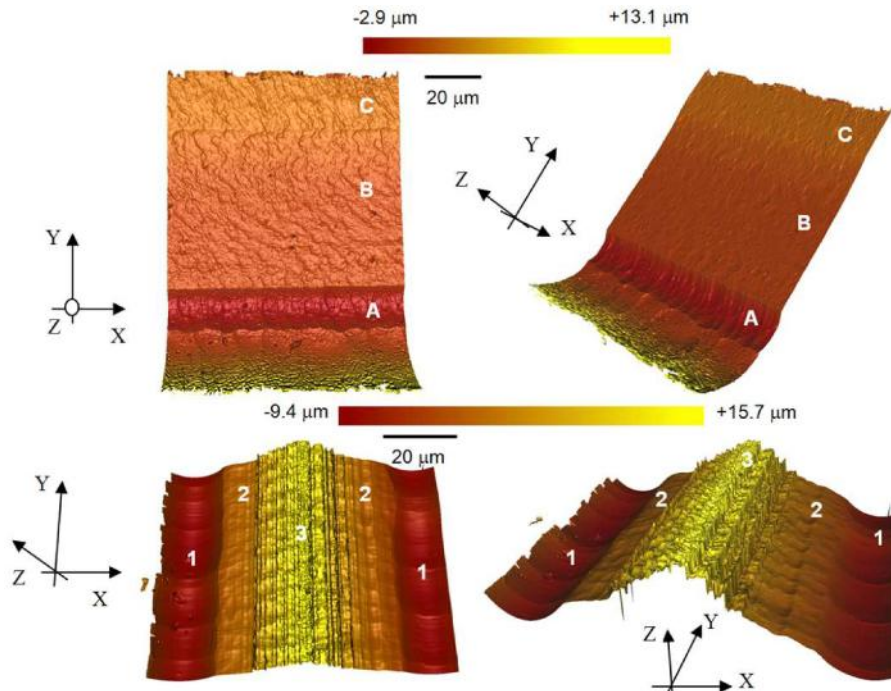


Fig. 7. High resolution confocal scanning microscopy (CSM) 3D surface topography maps of PDMS moldings of silica samples after femtosecond laser machining. The data was inverted to reveal the 'actual' silica mold surface topography. Top: side wall of a microchannel made in a silica block, the lower part reaches down to the channel floor. Bottom: channel floor. It was rotated by 90° relative to its real orientation in order for the general profile to stand out better. The topography varies across the length and width of the areas presented here, showing regions of varied corrugation (1, 2, 3).

The channel side wall reveals that: the surface texture parameters of region A are affected by the large round ditch-like feature created by the fabrication process, which results in high waviness and roughness (see the Table 1 caption for details) and presents an ‘in between basin step’ while the feature spacing equals about 4 μm . Regions B and C have the same roughness and spacing, respectively 40 nm and 3 μm , which indicates similar laser-matter interaction in spite of the subtle step-like boundary between them.

The channel floor clearly presents three different regions which all have a lot of form and waviness. Their roughness is also significant: higher than 400 nm and even 900 nm in region 3 (centre of the channel floor). Contrary to the side walls, the channel floor does not exhibit the same sort of micron-sized features one sees on the walls unless they are masked by another sort of sharper superimposed linear corrugation (as seen in Fig. 6 and 7). Only bowl-shaped, 10 μm -wide and 14 μm -apart cells appear in region 1, while region 2 presents cells which are 8 μm apart and elongated along the x-direction. As for region 3, the chaotic nature of this area – according to our CSM surface maps – rendered grain analysis futile.

Figure 8 shows the reconstructed cross-section profile based on the CSM data. Only one sidewall was measured but there is an obvious mirror-symmetry of the profile with respect to the central portion of the channel.

Table 1. Quantitative analysis of the corrugation of silica surfaces after exposure to fs-laser beam and HF etching through the surface metrology of their PDMS moldings. Iq is the rms roughness (height parameter only) of the ‘raw’, unprocessed map; Wq corresponds to the ‘waviness’, i.e. the surface topography after removal of a best-fit plane and applying a low pass filter in the spatial frequency domain (Fourier analysis): waves of length shorter than $\lambda_{low} = 11 \mu\text{m}$ were filtered out; Rq is the ‘roughness’, i.e. rapid variations in topography for waves of length shorter than λ_{low} and longer than $\lambda_{high} = 0.6 \mu\text{m}$, anything shorter than that was considered to reflect unwanted noise in the data and thus filtered out; *spacing* is the average distance between characteristic features that are enhanced by Fourier analysis in the ‘roughness’ map (grain analysis).

Areas	Iq (nm)	Wq (nm)	Rq (nm)	Spacing (μm)
A	1523	1099	396	4.3
B	160	137	42	3.1
C	85	54	42	3
1	1474	980	459	14
2	1360	916	412	8.1
3	3374	2850	915	-

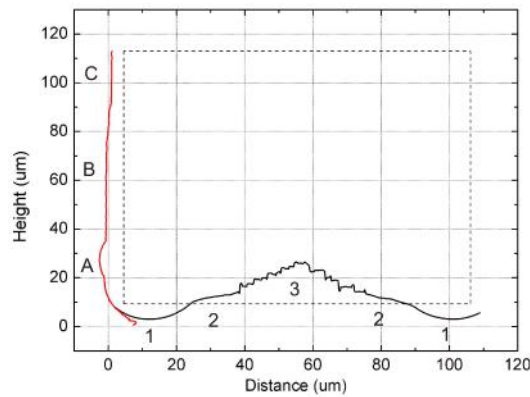


Fig. 8. Stitched vertical (red) and bottom measured cross-section profile of the channel (black). The dotted lines represent the desired initial pattern. References to the regions of interest described in Fig. 6 and 7 as well as Table 1 are highlighted.

5. Discussions

From the deviation from the desired profile (dotted-line in Fig. 8), we note the following facts:

1/ the laser-exposed profile has a U-shape. The etchant has therefore progressed from point C to A (and its mirror counterpart) and then from 1 to 3.

2/ the roughness increases from region C to A and from 1 to 3, which is consistent with the path followed by the etchant. (Regions with lower roughness were exposed for a longer time to the etchant.)

3/ although C was exposed to the etchant for a longer time, the deviation from the desired profile is much less pronounced there than it is at the bottom-corner (regions A and 1) that was exposed for a shorter time. It means that the etching rate, *outside the laser-affected zone proper*, was not constant from C to A and that this etching rate was actually faster at the bottom-corner.

4/ regions A and 1 in the etched profile (shown in Fig. 7 and 8) form a quasi-circular profile with a radius of about 15 μm . This quasi-circular profile is also particularly visible in the SEM images (Fig. 6 - insets 2 and 3).

5/ the central region (i.e. region 3 in Fig. 7 and 8) presents periodic patterns that match the periodicity of the laser-affected zones.

The simple fact that etching rates were not constant outside the laser-exposed area is very interesting. It shows that another mechanism than direct laser exposure caused an increase in etching rate.

For regions outside the laser-exposed area, the only mechanism that can lead to an etching rate increase is the presence of stress. It is widely accepted that the fused silica matrix consists of SiO_4 tetrahedra forming ring structures of different sizes [34] (a summary of the properties of Si-O-Si bonds is proposed in [37]). From M. Tomozawa *et al.* [35], tensile stress induces a change of bonding angle in SiO_4 groups. This change in bond angle also brings about a change in etching properties, and in particular etching rate [36]. Therefore, the corners (regions A and 1) were under significant tensile stress. The question that arises is: what could possibly explain the presence of this stress?

Our previous observations [9, 16, 32] as well as those of others [38, 39] suggest that a femtosecond laser induces a localized densification of the material in the laser-exposed area. Furthermore, we have observed a clearly defined boundary between densified and non-densified zones as indicated by observations reported in [9] and [16]. Considering these two facts, for the material to be in mechanical equilibrium, a tensile stress gradient must surround laser-affected zones so as to relax the local change in volume. Moreover, the presence of stress-induced birefringence extending from about a few microns from the laser-affected zones was reported in [32].

To test the stress-hypothesis, we have simulated the stress distribution around the laser-affected zones (Fig. 9) using a commercial finite element analysis software (COMSOL). We consider a linearly elastic plane-stress problem which is equivalent to assume an infinitely long channel. In this model, we model individual laser-affected zone (LAZ) that are caused by low-energy pulses as a continuous volume having an elliptical shape stretched along the laser propagation axis. We justify this choice by systematic scanning thermal microscope observations [16] that revealed clear images of LAZ cross-sections. Note that theoretical modeling of the non-linear laser-matter interaction by Rayner *et al.* [40] also predicts an elliptical shape at low-pulse energy levels. The small and long axes dimensions of the ellipse (8 μm x 1 μm) were taken from [16] according to the confocal parameters of the laser and pulse energy being used. After exposure, we assume that the elliptical zone has a higher Young modulus than the bulk does. For the simulation, we consider a Young modulus of 75 GPa (as opposed to 72 GPa for the bulk) based on our nanoindentation measurements [32] on laser-affected patterns. To simulate the stress resulting from densification, we assume that each of the LAZs is subject to a 150 MPa-homogeneously distributed pressure as it is suggested by our observations of stress-induced birefringence [32]. We then assume that the material

responds linearly to this stress, which is fair given the nature of the material being considered (no plasticity). To estimate the global stress distribution in the channel, we construct an exact replica of the pattern that was written with the laser by positioning an elliptical LAZ at each location where the laser was focused. Considering the elongated shape of the channel (several mm long), the problem was formulated as a plane-strain analysis.

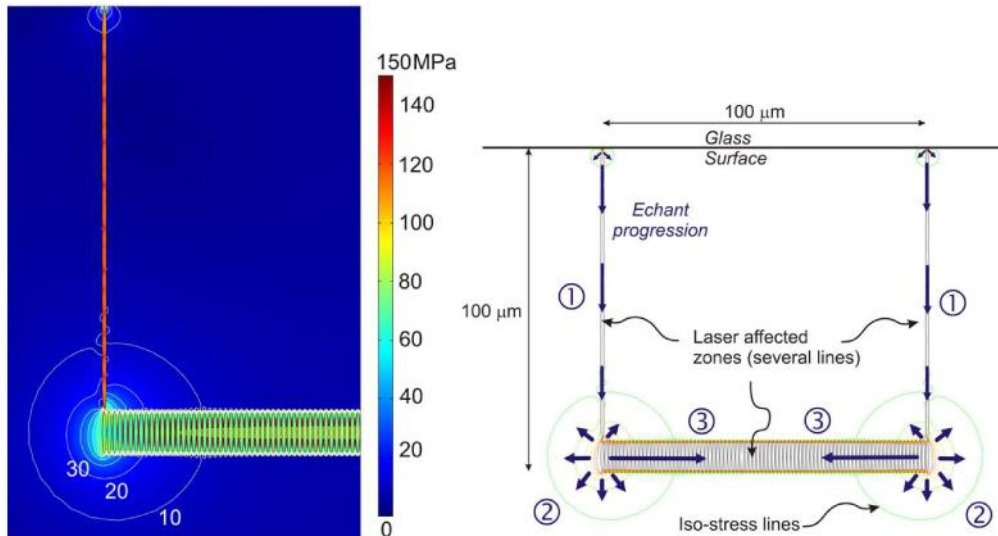


Fig. 9. Left: Cross-sectional map of the simulated stress distribution in the channel after laser exposure. Considering the symmetry of the problem, only the left half of the structure is being calculated in order to reduce computing time. The positions of the laser-affected zones strictly follow the programmed pattern that was written into the glass. Right: Channel geometry and etching front progression hypothesis.

Figure 9 (left) shows a cross-sectional map of the simulated stress distribution around the laser affected zones. The laser-written pattern consisted of two areas: the channel walls (region 1 in Fig. 9 right) generated by overlapping multiple laser-affected zones and the channel floor made up of several LAZs placed next to one another (region 3 in Fig. 9 left). Figure 10 shows the stress profile around the corners of the structure. The stress relaxation as we move away from the laser-exposed area is clearly visible. Interestingly, the simulation predicts stress concentration with circular profiles (see iso-stress contours in Fig. 9) at the corners of the pattern, precisely where this rounded profile was found (region 1 in Fig. 8). In terms of etching, one would expect the etched boundary to progress in a direction normal to the iso-stress contours, moving from areas subjected to higher stress to areas subjected to lower stress as shown in Fig. 9, right. Looking at the iso-stress line profile (Fig. 10), there are indeed striking similarities with the observed topographic profile of the channel after etching (see for instance Fig. 6 and 7). In our opinion, these results validate two hypotheses:

1/ laser-affected zones are indeed densified

2/ the etching of femtosecond laser-written patterns is driven by both the direct laser-induced upsetting of the material matrix and by the presence of high-stress around it. As a consequence and for the pulse energy levels considered in this work, these results exclude the presence of nanocracks as the cause for the enhanced etching rate. If such nanocracks had been present, the surrounding stress would have been removed and the final profile would be more tapered channels.

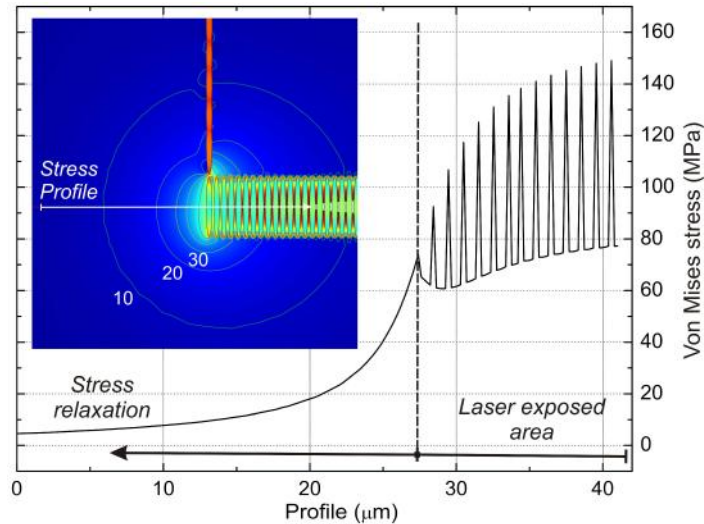


Fig. 10. Stress distribution across the bottom-left corner of the channel's laser pattern. The inset map shows the location where the stress profile is plotted. The oscillations visible in the laser exposed area correspond to the stress in between two laser-affected zones.

6. Summary

The contribution of this paper to the research on femtosecond laser micromachining is multifold:

1/ we have demonstrated the use of three-dimensional femtosecond laser-micromachining to create patterned silica surfaces with shallow microbasins or fused silica molds with moderate to high aspect ratio holes. Here, we tested elastomeric PDMS as molding material but many other materials could be utilized, not necessarily of polymeric nature. Thanks to the use of simple - i.e., accessible to a non-chemist - but adjustable and relevant ultrathin release coatings of appropriate non-adhesive and non-frictional properties which play an essential role for de-molding, we showed that aspect ratios of at least ten-to-one can be achieved. The accuracy of so-obtained PDMS moldings is of the order of 5 nm.

2/ to illustrate the possibly quite universal nature of our molding process, we applied it to structures such as holes and channels. There, we showed that the use of moldings offers an elegant, non-destructive method to quantitatively assess the surface texture and geometrical characteristics of deep structures. For the first time, we are capable of observing the inner surface of deep narrow blind holes of a few microns in diameter.

3/ finally, the molding of complex structures like channels formed by the juxtaposition of multiple laser-affected zones gave us a unique opportunity to investigate the underlying mechanisms responsible for the etching of silica-exposed 'patterns' to femtosecond lasers. On this particular topic, we demonstrate the importance of the stress distribution for the etching of complex patterns after exposure to femtosecond lasers.

Acknowledgements

The authors would like to thank Emeline Bourdel for helping out with the molding experiments. This research was supported by the European Commission through the NMP division of the 6th Framework Programme (Project GOLEM, no 033211) and the 7th Framework Programme (Project FEMTOPRINT, no 260103).